Available online at www.sciencedirect.com

SCIENCE DIRECT®

Earth and Planetary Science Letters 232 (2005) 39–49

EPSL

www.elsevier.com/locate/epsl

The 1998 Aiquile, Bolivia earthquake: A seismically active fault revealed with InSAR

Gareth J. Funning[a,*], Richard M.D. Barke[a,1], Simon H. Lamb[a], Estela Minaya[b], Barry Parsons[a], Tim J. Wright[a]

[a]*Department of Earth Sciences, University of Oxford, Parks Road, Oxford OX1 3PR, UK*
[b]*Observatorio San Calixto, Calle Indaburo 944, Casilla 12656, La Paz, Bolivia*

Received 14 June 2004; received in revised form 6 December 2004; accepted 6 January 2005

Editor: S. King

Abstract

Using SAR interferometry (InSAR), the deformation field of the M_w=6.6, 1998 Aiquile, Bolivia earthquake is mapped, and the epicentre accurately located for the first time. Elastic dislocation modelling is used to demonstrate that the measured displacements are best explained with a ~N–S oriented fault, with a strike that is oblique to the principal topographic features in the region, and a location that agrees with a Modified Mercalli Intensity map constructed from observations of damage in the surrounding area. A variable-slip solution for a fault in this orientation is obtained which predicts peak slip of 1.42 m at depths of ~4–5 km on the fault plane and has an estimated seismic moment, M_0=8.44×10^{18} N m, which agrees with estimates from long-period seismology. This is the first time that a fault has been demonstrated unambiguously to be active in the Central Andes, and since there was no previous knowledge of an active fault with this location or orientation, a necessary conclusion is that our understanding of seismic hazard in this region is limited.

Keywords: InSAR; earthquake; Bolivia; elastic dislocation modelling; source parameters

1. Introduction

The town of Aiquile is situated in the Eastern Cordillera of the Bolivian Andes, between the actively shortening fold-and-thrust belt of the Sub-Andes and the high plateau of the Altiplano (Fig. 1, [1]). Folding and thrusting ceased in the Eastern Cordillera in the late Miocene, around 10 Ma [2,3]; however, the region lies

* Corresponding author. Tel.: +44 1865 272066; fax: +44 1865 272072.
E-mail address: garethf@earth.ox.ac.uk (G.J. Funning).
[1] Present address: ExxonMobil North Sea Production, Grampian House, Union Row, Aberdeen, UK.

0012-821X/$ - see front matter © 2005 Elsevier B.V. All rights reserved.
doi:10.1016/j.epsl.2005.01.013

in the core, or 'hinge zone', of the Bolivian Orocline, and palaeo-magnetic studies and observations of shortening gradients and the pattern of active deformation along the Sub-Andes suggest that relative rotations have occurred in the region in the last 10 My [4–8]. There are several means by which these relative rotations could be accommodated—for instance, by conjugate strike-slip faulting in the hinge zone or by tangential extension along the outer bend of the orocline [7,9].

The topography of the area is dominated by a series of subparallel ridges of intensely deformed Palaeozoic clastic sediments striking predominantly N–S in the southern limb of the orocline and WNW–ESE in the northern limb of the orocline, mirroring the larger-scale changes in strike of the mountain chain. There are steep changes in elevation across the area on several length scales. The total elevation change from the foreland in the east to the edge of the high Altiplano to the west is approximately 3500 m over 200 km, with around 2000 m of this relief across the study area. Locally, individual ridges can rise 500–750 m above their neighbouring valleys over distances of just a few kilometres. It is possible to identify many strong lineations in this topography, many of which have

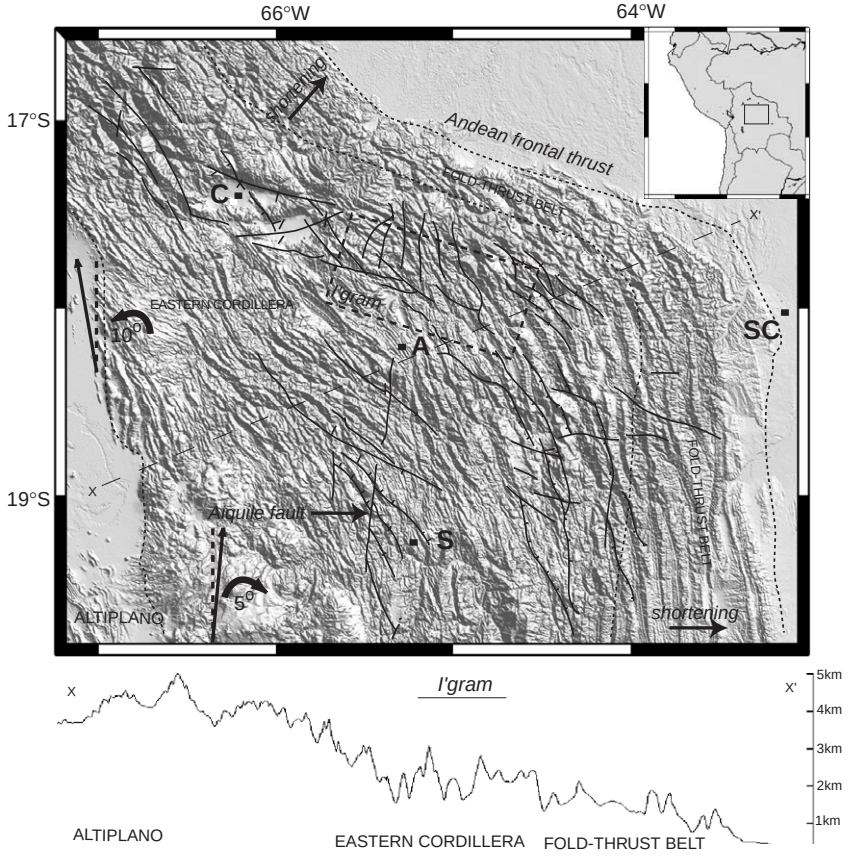

Fig. 1. Simplified tectonic map of the Central Andes, overlaid upon shaded relief topography. The Altiplano, Eastern Cordillera and Sub-Andean fold-and-thrust belt are delineated. Shortening is focussed in the fold-and-thrust belt in the directions marked, measured palaeomagnetic rotations [6] indicate the motion of the hinge zone since 10 Ma. Mapped lineations in the topography [10] are marked with solid lines; however, to date, none have been confirmed to be currently active. The area covered by the coherent portion of the SAR interferogram is outlined (dashed box). A topographic profile shows the steep changes in relief across the area, and across the interferogram (labelled I'gram). Topography is taken from the 90 m SRTM dataset. A=Aiquile, C=Cochabamba, S=Sucre, SC=Santa Cruz.

been mapped as faults ([10], Fig. 1). Although there is evidence to suggest Plio-Pleistocene-age sinistral strike-slip faulting on the E–W-trending Cochabamba–Tapacari Lineament to the northwest [9], and possible post-folding and thrusting-age dextral strike-slip motion on the N–S-trending Aiquile Fault to the south [1], conclusive evidence of active faulting such as earthquake motions or offsets has not been observed on any of the lineaments in the hinge zone, despite moderate levels of shallow seismicity (e.g. [11]).

The prime obstacle to demonstrating which faults accommodate active deformation in the region is the lack of reliable seismic event locations for earthquakes in the Central Andes. Instrumentation is sparse, and local crustal velocity models are poorly determined, complicated by the large changes of elevation and crustal thickness across the region [12]. Without a consensus as to the precise location of earthquakes in the Eastern Cordillera, it is not possible to tie events to potential fault structures. We present here the first study of a Bolivian earthquake using Interferometric Synthetic Aperture Radar (InSAR), a high-resolution space-based geodetic technique [13,14] which allows us to accurately locate a shallow Bolivian earthquake for the first time, and also to place constraints on the geometry of, and the distribution of slip upon, the fault on which it occurred.

2. The Aiquile earthquake: surface and seismic observations

On 22nd May 1998 at 04:48 (UT), a M_w=6.6 earthquake struck the Aiquile region, causing over 100 fatalities and widespread damage across an area approximately 100 km in diameter, and rendering thousands of families homeless. This was the largest shallow earthquake in Bolivia in over 50 years, and was felt as far away as the cities of Cochabamba and Sucre, approximately 100 km away.

The heaviest observed damage occurred in the village of Hoyadas—all 50 houses in the settlement were destroyed, and fissures up to 100 m long and 2 m deep were observed, both in the village graveyard and in the hills to the east. Surface cracking was also observed in and around several other settlements in the area, in some places in conjunction with changes in ground water (Table 1).

In addition, 75% of houses were destroyed or heavily damaged in the town of Aiquile. Damage here was largely confined to the central part of the town, built upon the unconsolidated sediments of an ancient alluvial system, suggesting that sub-surface geology played a role in accentuating seismic intensities. Similarly, the town of Totora to the north was more heavily damaged than its surrounding area—again this is likely to be due to the substratum

Table 1
Modified Mercalli Intensity observations of the Aiquile earthquake

Settlement	Lat.	Long.	Intensity	Observation
Hoyadas	−17.922	−65.168	VIII	Collapse of all adobe buildings, fissuring and sliding of sediment on hillsides.
Pampa Grande	−17.849	−65.170	VIII	Severe damage to all adobe buildings. Ground fissuring observed.
Totora	−17.731	−65.191	VII	70% of buildings damaged, some partially collapsed.
Chujllas	−17.990	−65.136	VII	Damage to buildings, fissuring and emanation of ground water.
Aiquile	−18.198	−65.179	VII	75% of buildings damaged, 46% partially collapsed.
Lambramani	−17.789	−65.197	VII	28 houses damaged, soil fissuring, fallen roof blocks.
Mizque	−17.938	−65.313	VI	Cracking in walls and floors of adobe buildings.
Keweña Khasa	−17.704	−65.532	VI	Cracks in walls of houses and bridge.
Tiraque Chico	−17.664	−65.094	VI	School, church tower and bridge heavily cracked.
Copachuncho	−17.546	−65.088	VI	Small cracks formed in houses.
Arani	−17.567	−65.767	V	Earthquakes felt, no building damage.
Pojo	−17.755	−64.863	V	Earthquakes felt, no building damage.

on which the town was constructed, as well as the age and manner of construction of the buildings, many of which dated back to the earliest settlement of the town in 1850.

These observations of damage, from these and other settlements (Table 1) have been used to compile a Modified Mercalli Intensity map of the strength of the shaking (Fig. 2). No surface features resembling a fault rupture were found, however, although a full search of the area was not possible due to the difficulty of access, both in terms of the terrain and the limited road network, and the limited numbers of personnel in the field.

Epicentral locations from various agencies are plotted in Fig. 2. There is little agreement between the locations and the observed intensities from damage reports, or between the seismic epicentres themselves. The various location estimates are distributed over a zone approximately 40 km across, making it difficult to identify the structure involved. The positions of the aftershocks are equally inconclusive, forming a diffuse 'cloud' of locations, which

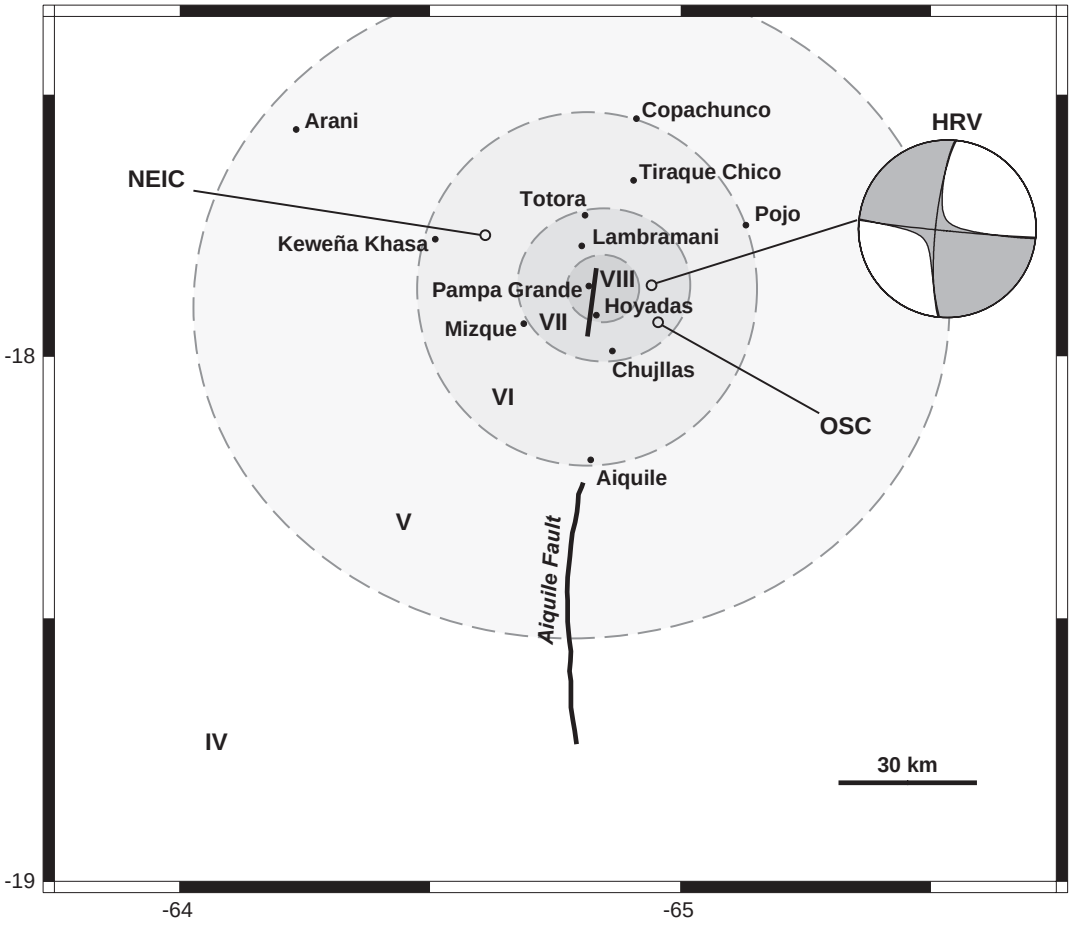

Fig. 2. Locations and observations of damage, and instrumental seismic locations for the Aiquile earthquke. Settlements in which observations of damage were made (Table 1) are plotted, with best-fitting isoseismals (dashed lines). Seismic locations are plotted as hollow circles (HRV=Harvard CMT, OSC=Observatorio San Calixto, NEIC=National Earthquake Information Centre). The Harvard CMT focal mechanism shown is consistent with dextral N–S or sinistral E–W strike-slip faulting. The Aiquile fault (curved solid line) and the fault model that best fits the InSAR data (straight solid line) are shown, the latter showing good agreement with the highest seismic intensities.

gives no clue as to the orientation of the fault plane. The focal mechanism, as determined by the Harvard Centroid Moment Tensor (CMT) method [15], is consistent with either right-lateral strike-slip on a subvertical N–S fault plane or left-lateral strike-slip on a vertical E–W fault plane. In the absence of any definite identification of a fault rupture on the ground, any pattern to the located aftershocks, or without further seismological analysis to determine rupture directivity (e.g. [16]), which is the actual fault plane cannot be determined.

3. Determining fault parameters using InSAR

Only one pair of SAR images with a suitable interferometric baseline and time interval exists within data archive of the European Remote Sensing (ERS)

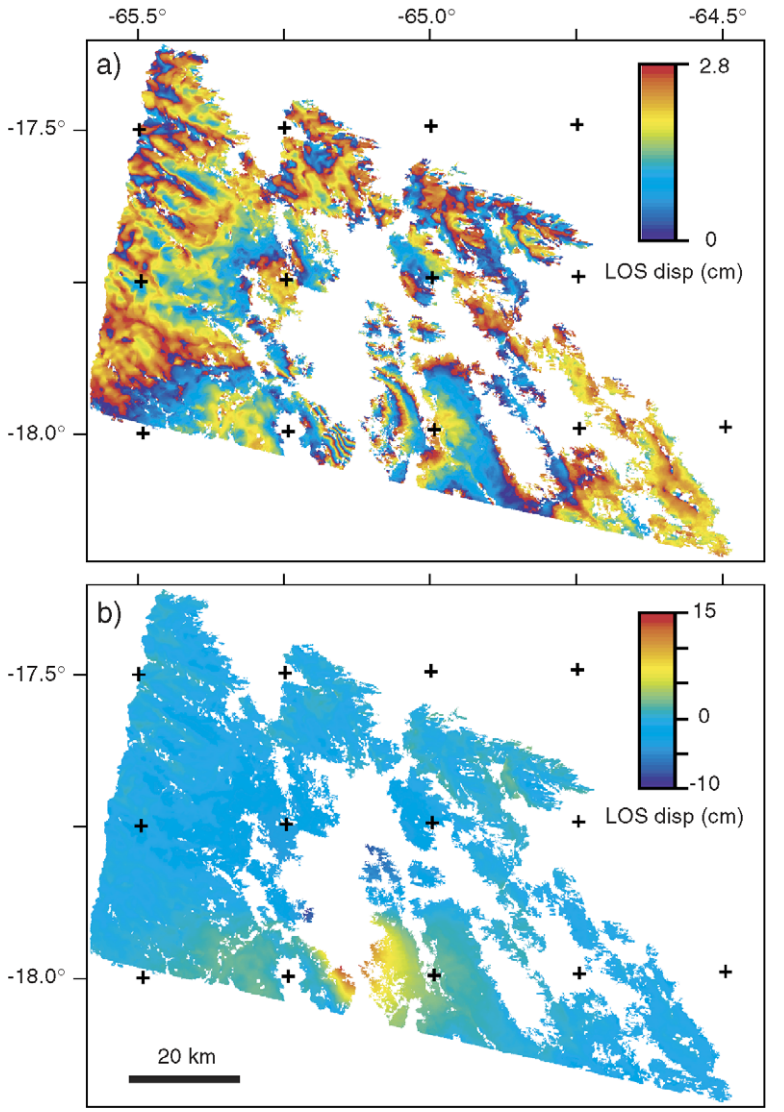

Fig. 3. (a) Wrapped interferogram of the Aiquile earthquake. Each cycle of blue–yellow–red is equivalent to a motion of 2.8 cm towards the satellite in its line-of-sight (LOS) direction. (b) Unwrapped interferogram. Positive LOS displacements are towards the satellite.

Table 2
Source parameters of the 22nd May 1998 Aiquile, Bolivia earthquake from various source models

Model	Data	Lat.	Long.	Depth[a]	M_0 (Nm)	Strike	Dip	Rake	Slip (m)	Length (km)	Width (km)	Rms misfit (mm)
Harvard CMT[b]	Seis.	−17.600°	−65.200°	15.0[c]	8.44×10^{18}	186°	79°	−178°	–	–	–	–
						96°	88°	−11°	–	–	–	–
Uniform slip, N–S	InSAR	−17.897°	−65.177°	7.4	7.77×10^{18}	7°	79°	171°	1.10	14.5	15.0	7.7
Uniform slip, E–W	InSAR	−17.898°	−65.183°	7.9	6.80×10^{18}	96°	74°	8°	3.20	4.0	16.5	9.3
Uniform slip, E–W[d]	InSAR	−17.887°	−65.185°	7.4	8.12×10^{18}	106°	63°	−5°	1.01	15.0[d]	16.5	11.8
Variable slip, N–S	InSAR	−17.897°	−65.177°	8.0	8.44×10^{18}	7°	79°	171°	1.42(0.60)[e]	24.0[f]	18.0[f]	6.6
Variable slip[g], N–S	InSAR	−17.897°	−65.177°	7.7	7.61×10^{18}	7°	79°	171°	1.57(0)[e]	23.0[f]	14.0[f]	7.5

[a] Centroid depth.
[b] Both nodal planes listed.
[c] Centroid depth fixed at 15 km.
[d] Fault length fixed at 15 km.
[e] Peak slip (maximum surface slip in parentheses).
[f] Dimensions of an area enclosed by a contour of slip within which 95% of the total slip occurred.
[g] Model constrained to have zero slip at the surface.

satellites.[2] This was processed with the JPL/Caltech ROI PAC (Repeat Orbit Interferometry Package) software [17] using a 3 arcsec (~90 m) resolution digital elevation model (DEM) generated by the NASA Shuttle Radar Topography Mission (SRTM) to correct for the topographic phase contribution. The final interferogram, after filtering [18], is shown in Fig. 3 in both wrapped and unwrapped forms. Only the coherent southern half of the interferogram is shown—as elevation decreases to the north, there is a major increase in vegetation, and therefore in temporal decorrelation, which obscures any signal from that area. However, a clear deformation signal can be seen in the coherent part of the image, with a peak-to-peak line-of-sight (LOS) displacement offset of ~25 cm, highlighting the potential of the technique to image deformation in rugged, semi-arid areas. To prepare the data for modelling, the interferometric phase was then resampled using a quadtree decomposition algorithm [19], a technique which concentrates sampling in areas of high phase gradients, thus reducing the number of datapoints to be modelled from ~1 million to 674.

For a first-order model, we wish to determine which of the two possible orientations of the fault plane is the correct one. Representing the fault as a rectangular dislocation in an elastic halfspace using the formulation of Okada [20], we model two scenarios—a 'N–S' fault, where the fault strike is allowed to vary between 320° and 040°, and an 'E–W' fault where the fault strike is allowed to vary between 050° and 130°. Fault parameters are systematically varied using a Powell minimization algorithm, using 100 Monte Carlo restarts, so that a global minimum misfit is found in each case [21]. In addition to solving for the main fault parameters (strike, dip, rake, slip, location, maximum and minimum depth), we solve for three nuisance parameters–a static shift in LOS displacement and gradients of displacement to the north and east–to account for ambiguities in the zero displacement-level, and along- and cross-track orbital errors, respectively.

Our results are given in Table 2, with synthetic and residual interferograms plotted in Fig. 4. The best-fitting fault model is oriented approximately N–S, with a length of 14.5 km and a root mean square (rms) misfit[3] of 7.7 mm. The best-fitting E–W fault model not only has a worse rms misfit (9.3 mm), but with a length of 4 km it has a slip-to-length ratio of 8×10^{-4}—an order of magnitude greater than values found for most earthquakes (e.g. [22]). The fit to data further degenerates (rms misfit=11.8 mm) if an EW fault with a length of 15 km, and therefore a smaller slip-to-length ratio, is used. Therefore, the

[2] Image 1: ERS-2, orbit 05103, acquired 96/04/11. Image 2: ERS-2, orbit 17127, acquired 98/07/30. Track 239 (descending), frame 3962, perpendicular baseline 15 m, altitude of ambiguity 648 m.

[3] If d_i are modelled displacements and c_i are observed displacements, then the rms misfit is given by $\sqrt{\frac{1}{N}\sum_{i=1}^{N}(d_i-c_i)^2}$, where N is the number of datapoints.

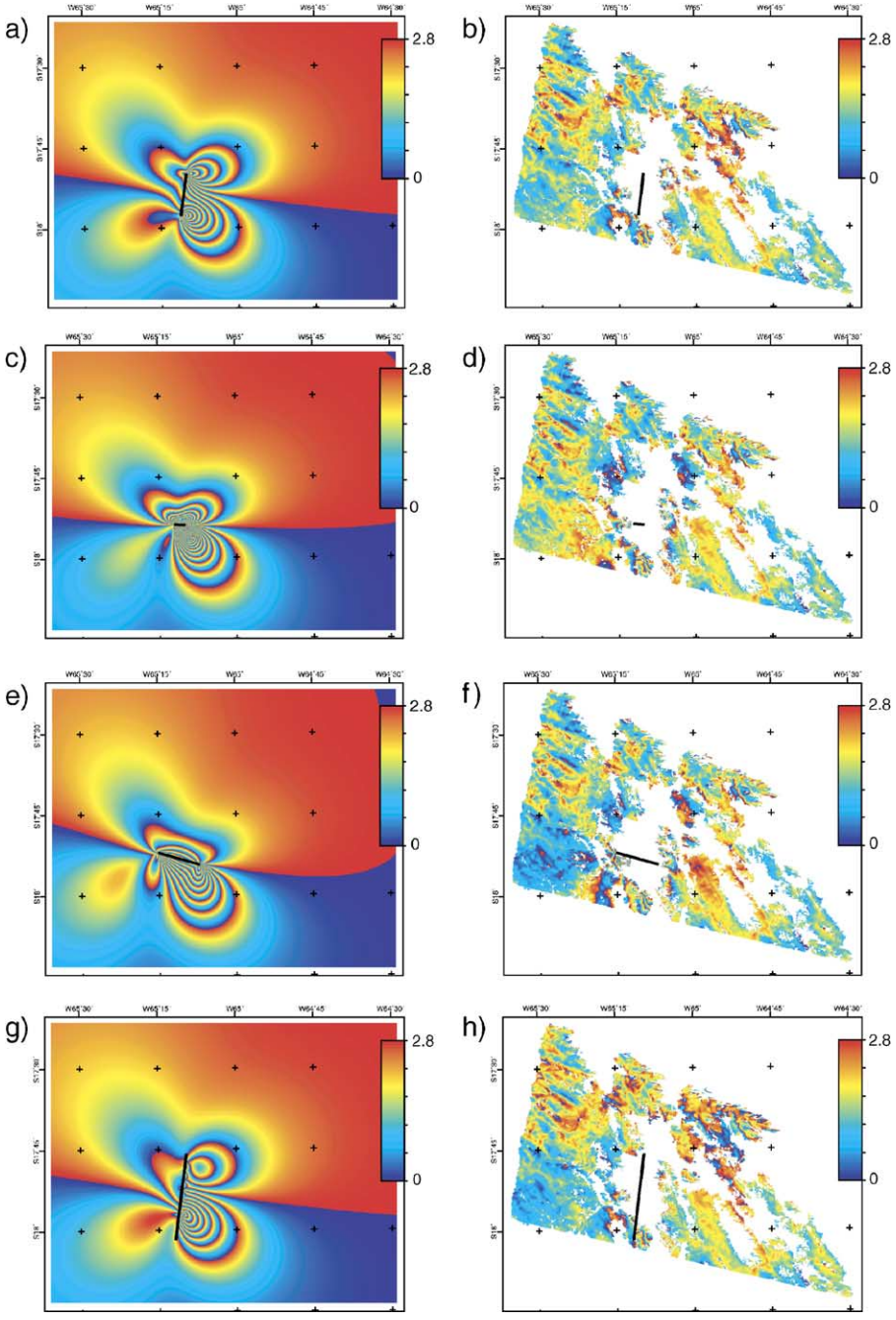

Fig. 4. Synthetic interferograms (a, c, e, g) and residual interferograms (b, d, f, h) for different source models of the Aiquile earthquake: (a, b) best-fitting uniform-slip N–S fault; (c, d) best-fitting uniform-slip E–W fault with unrealistic slip-to-length ratio; (e, f) a longer uniform-slip E–W fault with a more realistic slip-to-length ratio; (g, h) enlarged N–S fault with distributed slip. Surface fault traces are marked as thick black lines. Linear trends corresponding to calculated nuisance parameters have been removed. Area shown and colour scheme as for Fig. 3a above.

initial modelling results are strongly in favour of a fault with a N–S orientation. This fault model agrees well with the Modified Mercalli Intensity map based on surface observations, plotting in the zone of the highest intensities (Fig. 2), and has a strike very close to that of the Harvard CMT solution (Fig. 2, Table 2).

The N–S fault model can be further refined by solving for the distribution of slip on the fault. We extend the fault in the along-strike and down-dip directions, increasing its total length to 30 km and down-dip width to 21 km, parameterising the fault into a series of smaller 1×1 km subfaults. With a fixed fault geometry, it is then a simple linear problem to invert the InSAR data for the slip on each subfault. To prevent unphysical oscillatory slip and retrograde motion on the fault in our solutions, we impose Laplacian smoothing and invert the data using a non-negative least-squares algorithm [23]. We fix the rake to the value obtained for the first-order model above, and solve for three nuisance parameters as before. Datapoints within 2 km of the surface trace of the fault are excluded to prevent biasing of the model by large data misfits close to the fault.

The slip distribution obtained is shown in Fig. 5a. Slip is arranged in an elliptical pattern and is concentrated in the central portion of the fault, peaking at 1.42 m at depths of ~4–5 km. There is a maximum of 0.60 m of slip within the upper, near-surface kilometre of the fault. Our variable-slip model shows an improved fit to the data in the residual plot (Fig. 4h) and in terms of its rms misfit of 6.6 mm, close to the level of noise in the data in the far-field. In addition, the model seismic moment of 8.44×10^{18} N m agrees with the Harvard CMT moment (Table 2). Many of the remaining, residual LOS displacements are almost certainly due to a difference in tropospheric water vapour content between the two image acquisitions—this is especially pronounced in the NW where individual valleys can be distinguished in the residual plot.

The degree of slip predicted in the upper kilometre of the fault should be detectable on the ground;

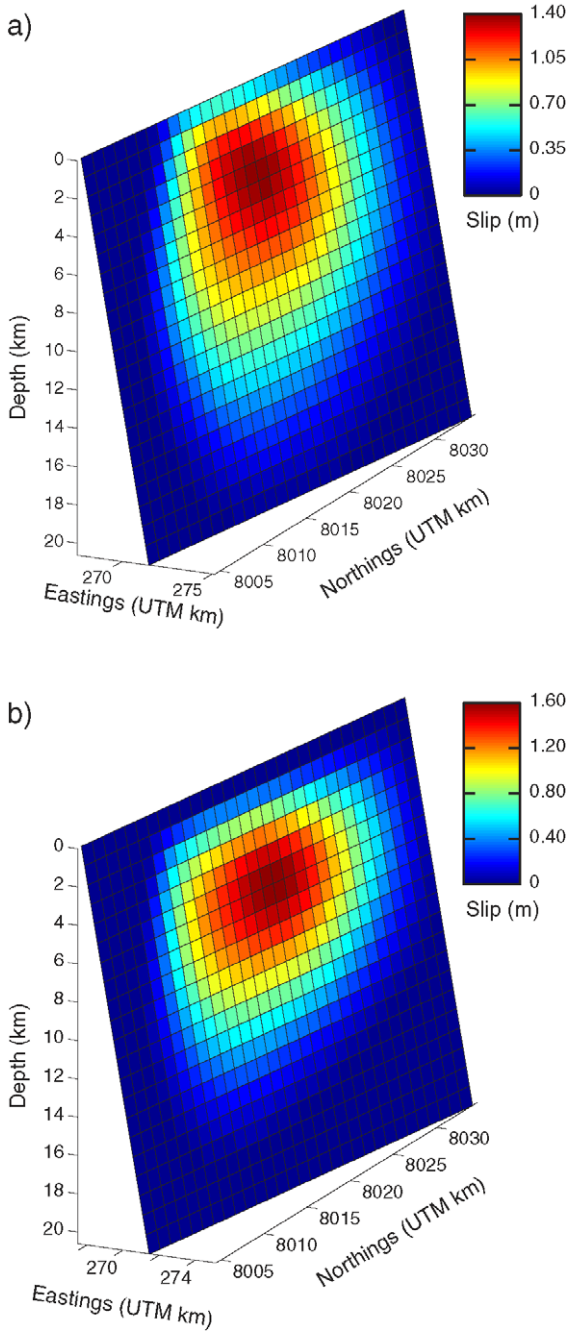

Fig. 5. Distribution of fault slip for two variable-slip models of the Aiquile earthquake. Horizontal coordinates quoted are in km, projected into Universal Transverse Mercator (UTM) coordinates (zone 20S). (a) Variable-slip model with no surface slip constraint. The overall pattern of slip is elliptical. Peak slip is 1.42 m in the depth range 4–5 km, with a maximum of 0.60 m of movement in the upper kilometre of the fault. (b) Variable-slip model where surface slip is constrained to be zero. An elongate elliptical pattern of slip is obtained, peaking at 1.57 m of slip in the depth range 5–7 km.

however, no surface rupture has been observed in the area. To test whether the data require high slip near the surface, we repeated the variable slip modelling, imposing the additional constraint that slip in the upper kilometre of the fault must be zero. The resulting pattern of slip (Fig. 5b) is also elliptical in shape, but 4 km narrower in width and with a higher peak slip of 1.57 m at depths between ~5 and 7 km. The fit to the data is marginally degraded for this model, with an rms misfit of 7.5 mm—~13% higher than that for the unconstrained inversion (Table 2), a difference that is probably not significant. We therefore believe that although the data prefer slip in the near-surface area of the fault, it is plausible that slip at the surface may not have occurred. In other words, we cannot tell with confidence whether the lack of an observed surface rupture is due to the difficulty of finding a small strike-slip surface offset in this extremely rugged and remote region, or because slip on the fault petered out to zero just below the surface.

4. Discussion

The observation of N–S right-lateral faulting in the area north of Aiquile has important implications for the mechanism of deformation within the hinge

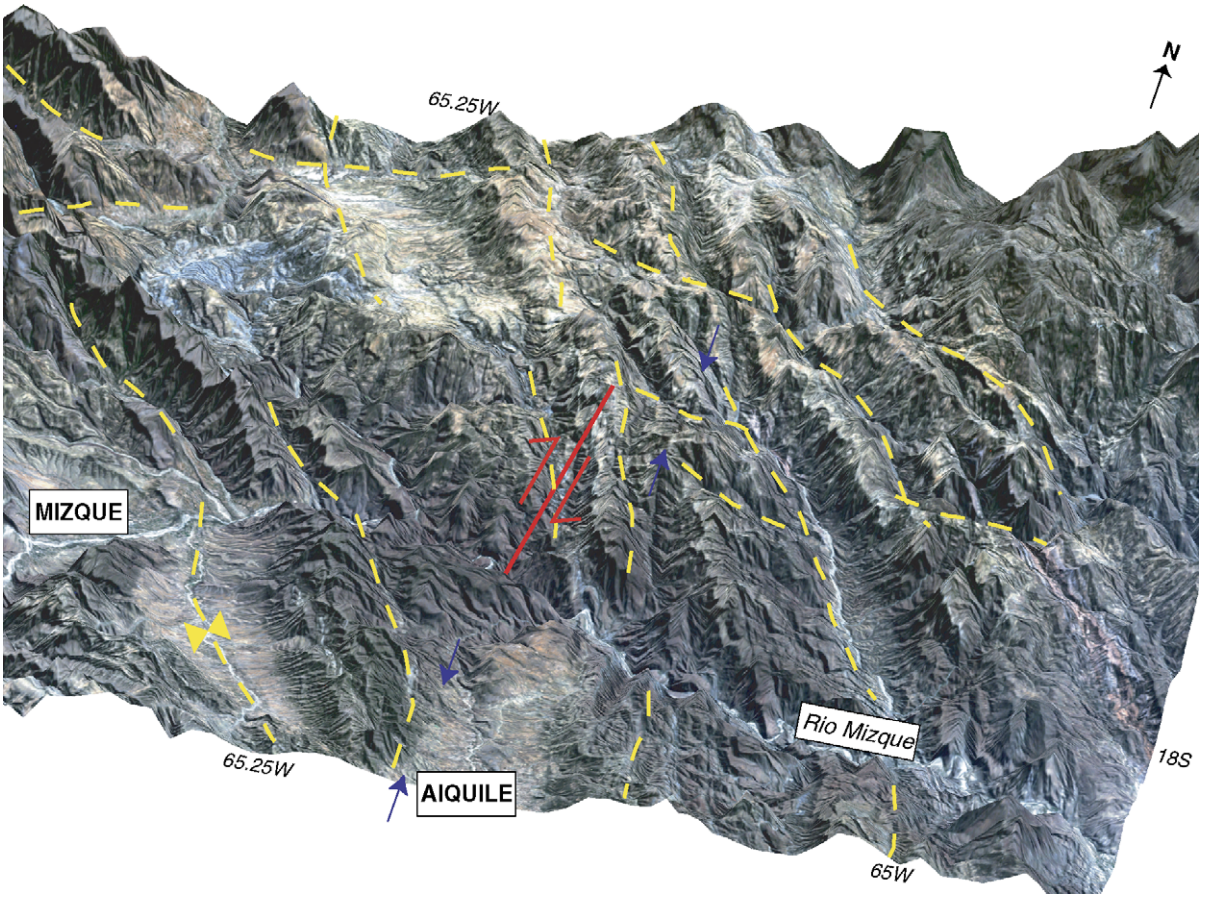

Fig. 6. LANDSAT-7 false-colour (321) image of the Aiquile area overlaid upon SRTM 90 m topography in perspective view. Red line represents the surface trace of the fault identified from the InSAR observations, significantly oblique to previously mapped topographic lineations, marked in yellow (R.M.D. Barke, unpublished field observations 2001–3, [10]). Blue arrows indicate topographic features with a similar strike to the active fault.

of the Bolivian Orocline. Coupled with observations of Quaternary left-lateral shear on an E–W-trending lineament in the Cochabamba region [9], this evidence suggests that the hinge zone of the orocline is deforming actively by conjugate strike-slip faulting. It is also possible to draw some conclusions about the size and nature of the faults upon which this faulting must occur. In the case of the Aiquile earthquake, the modelled fault cross-cuts the existing topography and has no obvious topographic expression (Fig. 6), suggesting that the fault is relatively young. Coupled with the absence, in the topography, of clearly defined large faults with kilometre-scale offsets in the hinge zone, it is possible to infer that the deformation in this area must occur on smaller-scale faults without obvious surface features. Indeed, the topography is dominated in this area by inactive ridges formed by fold-and-thrust-style deformation prior to 10 Ma [24], similar features to which further south in the Eastern Cordillera are cross-cut and offset by strike-slip faults [5,6], and therefore may not reflect current styles of faulting at all. Since much of our knowledge of faults in this region is based upon interpretation of topographic features [10], this discovery has important implications for seismic hazard in central Bolivia.

Our findings may also provide an important calibration of the in situ deviatoric stresses in this part of the Andes. The presence of a known active strike-slip fault at this elevation may indicate a changeover from thrusting and crustal thickening along N–S- or NW–SE-striking faults, with the intermediate stress, σ_2, horizontal in the Sub-Andes at elevations less than 2 km, to conjugate strike-slip faulting, with σ_2 vertical, at elevations greater than 2 km [5].

The success in processing InSAR data for the Aiquile earthquake shows us that, with the provision of a DEM of sufficient resolution and accuracy, it is possible to generate interferograms in remote areas with large changes in relief. The release of global 3 arcsec topographic data from the SRTM project should allow the study of similar events elsewhere. Such studies would be important for locating seismogenic faults whose locations were previously not well known and be valuable for our understanding of seismic hazards and regional tectonics in this and other such regions.

Acknowledgements

This work was supported by the Natural Environment Research Council through funding of the Centre for the Observation and Modelling of Earthquakes and Tectonics, a research studentship (GJF), a research grant (SHL) with tied studentship (RMDB), and a research fellowship (TJW). Support was also provided by grants from the EU and Royal Society (SHL) and a Hertford College Senior Scholarship (GJF). Thanks to Juan-Carlos James for providing valuable help in the field. Roland Bürgmann made helpful suggestions that have improved the manuscript. All SAR data is copyrighted by the European Space Agency. Some figures were prepared using the public domain Generic Mapping Tools [25].

References

[1] J.F. Dewey, S.H. Lamb, Active tectonics of the Andes, Tectonophysics 205 (1992) 79–95.
[2] T. Gubbels, B. Isacks, E. Farrar, High-level surfaces, plateau uplift, and foreland development, Bolivian Central Andes, Geology 21 (1993) 695–698.
[3] L. Kennan, S. Lamb, L. Hoke, High-altitude palaeosurfaces in the Bolivian Andes: evidence for late Cenozoic surface uplift, in: M. Widdowson (Ed.), Palaeosurfaces: Recognition, Reconstruction and Palaeoenvironmental Interpretation, Geol. Soc. Special Publ., vol. 120, 1997, pp. 307–323.
[4] J. Kley, Geologic and geometric constraints on a kinematic model of the Bolivian Orocline, J. South Am. Earth Sci. 12 (1999) 221–235.
[5] S. Lamb, Active deformation in the Bolivian Andes, South America, J. Geophys. Res., (Ser. B) 105 (2000) 25627–25653.
[6] S. Lamb, Vertical axis rotation in the Bolivian orocline, South America: 1. Paleomagnetic analysis of Cretaceous and Cenozoic rocks, J. Geophys. Res. (Ser. B) 106 (2001) 26605–26632.
[7] S. Lamb, Vertical axis rotation in the Bolivian orocline, South America: 2. Kinematic and dynamical implications, J. Geophys. Res. (Ser. B) 106 (2001) 26633–26653.
[8] N. McQuarrie, Initial plate geometry, shortening variations, and evolution of the Bolivian Orocline, Geology 30 (2002) 867–870.
[9] L. Kennan, Cenozoic tectonics of the central Bolivian Andes, PhD thesis, University of Oxford, Oxford, UK, 1994.
[10] J. Pareja, C. Vargas, R. Suarez, R. Ballon, R. Carrasco, C. Villarroel, Mapa geologico de Bolivia y memoria explicativa, scale 1:1000000, Yacimientos Petroliferos Fiscales Bolivianos y Servicio Geologico de Bolivia, La Paz, 1978.
[11] A. Vega, E. Buforn, Focal mechanisms of intraplate earthquakes in Bolivia, South America, Pure Appl. Geophys. 136 (1991) 449–458.

[12] S.L. Beck, G. Zandt, S.C. Myers, T.C. Wallace, P.G. Silver, L. Drake, Crustal-thickness variations in the central Andes, Geology 24 (1996) 407–410.
[13] D. Massonnet, K.L. Feigl, Radar interferometry and its application to changes in the earth's surface, Rev. Geophys. 36 (1998) 441–500.
[14] R. Burgmann, P. Rosen, E. Fielding, Synthetic aperture radar to measure earth's surface topography and its deformation, Annu. Rev. Earth Planet. Sci. 28 (2000) 169–209.
[15] A. Dziewonski, T.-A. Chou, J. Woodhouse, Determination of earthquake source parameters from waveform data for studies of global and regional seismicity, J. Geophys. Res. (Ser. B) 86 (1981) 2825–2852.
[16] J.J. McGuire, Estimating finite source properties of small earthquake ruptures, Bull. Seismol. Soc. Am. 94 (2004) 377–393.
[17] P.A. Rosen, S. Hensley, G. Peltzer, M. Simons, Updated repeat orbit interferometry package released, Eos Trans. AGU 85 (2004) 35.
[18] R.M. Goldstein, C.L. Werner, Radar interferogram filtering for geophysical applications, Geophys. Res. Lett. 25 (1998) 4035–4038.
[19] S. Jonsson, H. Zebker, P. Segall, F. Amelung, Fault slip distribution of the Mw 7.2 Hector Mine earthquake estimated from satellite radar and GPS measurements, Bull. Seismol. Soc. Am. 92 (2002) 1377–1389.
[20] Y. Okada, Surface deformation due to shear and tensile faults in a half-space, Bull. Seismol. Soc. Am. 75 (1985) 1135–1154.
[21] T.J. Wright, B. Parsons, J. Jackson, M. Haynes, E. Fielding, P. England, P. Clarke, Source parameters of the 1 October 1995 Dinar (Turkey) earthquake from SAR interferometry and seismic bodywave modelling, Earth Planet. Sci. Lett. 172 (1999) 23–37.
[22] C. Scholz, The Mechanics of Earthquakes and Faulting, Cambridge University Press, Cambridge, 1990.
[23] R. Bro, S. De Jong, A fast non-negativity-constrained least squares algorithm, J. Chemom. 11 (1997) 392–401.
[24] J.-P. Muller, J. Kley, V. Jacobshagen, Structure and cenozoic kinematics of the Eastern Cordillera, southern Bolivia, Tectonics 21 (2002) 1037, doi:10.1029/2001TC001340.
[25] P. Wessel, W.H.F. Smith, New, improved version of generic mapping tools released, Eos Trans. AGU 79 (1998) 579.